

# Multi-Modal Building Inspection via Perceiver IO Fusion of Satellite and Street-Level Imagery

Niels Sombekke<sup>1</sup> Rob G.J. Wijnhoven<sup>2</sup> Martin R. Oswald<sup>1</sup>

<sup>1</sup>University of Amsterdam (UvA), Amsterdam, The Netherlands <sup>2</sup>Spotr, The Hague, The Netherlands

nielssombekke@gmail.com rob@spotr.ai m.r.oswald@uva.nl

## Abstract

We present a multi-modal classification framework that fuses satellite and street-level imagery through a Perceiver IO architecture operating on spatial patch tokens from a shared DINOv2 backbone. The design naturally handles a variable number of street-level views per building without padding or fixed-size pooling, and jointly predicts multi-label roof element and roof material classes. We construct a large-scale dataset of 32,135 buildings (61,672 segments) spanning ten countries, pairing satellite images with up to eight street-level views per segment and evaluating four masking strategies for isolating the target building. We propose an RGB-M masking strategy that appends the building footprint mask as a fourth input channel, providing a soft spatial prior that outperforms hard cropping across both modalities. The Perceiver IO fusion model improves over all other fusion strategies and yields substantial per-class gains for attributes visible from street level (e.g., +11.3 AP for slate, +1.3 AP for dormers), though the satellite-only baseline retains a slight advantage in macro-averaged mAP for classes that are predominantly visible from above. These results establish a scalable, flexible architecture for multi-modal building inspection that can accommodate heterogeneous inputs and multiple output tasks.

## 1. Introduction

Maintaining and insuring the built environment at national scale requires detailed knowledge of individual buildings: what materials cover the roof, which structural elements are present, and what condition they are in. Traditional inspection relies on labor-intensive site visits that are costly, slow, and prone to human error, while generating significant CO<sub>2</sub> emissions from repeated travel [27]. With the European building stock alone comprising over 200 million structures, 40% of the EU’s energy consumption and 36% of its greenhouse gas emissions [5], manual approaches simply cannot keep pace with the demand for up-to-date property informa-



Figure 1. Example input data for a building: satellite image (left) and corresponding street-level images (right). Satellite imagery captures roof geometry and context, while street-level views reveal facade details, materials, and structural elements that are invisible from above.

tion. A scalable, data-driven alternative is needed.

Remote sensing offers a scalable path. Satellite and aerial imagery can be collected over large areas, updated regularly, and processed algorithmically, enabling the analysis of thousands of properties without physical visits. Satellite data captures a building’s footprint, roof geometry, and surrounding context from above, while street-level imagery—increasingly available through services such as Google Street View—provides close-range views of facades, wall conditions, and material textures that are invisible from a top-down perspective. Combining both modalities can produce richer, multi-perspective building profiles than either source alone [2, 11, 22].

However, fusing satellite and street-level imagery poses several challenges. First, the data itself is heterogeneous: satellite images may have limited resolution and suffer from misaligned building footprints, while street-level views are frequently occluded by vegetation, vehicles, or neighboring structures [10]. Second, an effective method must isolate the target building from its surroundings—leveraging the building footprint to focus on the relevant structure—while retaining enough environmental context to support classification. Third, the number of available street-level images varies widely across buildings: some have dozens of views from different angles, others have none at all. A practical architecture must therefore handle a variable number of inputs without degrading performance on buildings with sparse or missing street-level coverage.

We address these challenges with a Perceiver IO-based fusion architecture [15] that operates directly on spatial patch tokens extracted by a shared DINOv2 [26] backbone. Unlike feature-vector fusion approaches that discard spatial structure through global pooling, our model preserves fine-grained patch-level information from both modalities and compresses them through cross-attention into a fixed-size latent representation. The architecture naturally accommodates varying numbers of street-level inputs through its set-based cross-attention mechanism, and jointly predicts multi-label roof element and roof material classes via task-specific output heads.

We make the following contributions:

1. We develop a Perceiver IO fusion model that processes spatial tokens from satellite and street-level imagery, outperforming concatenation and transformer-based fusion baselines and delivering substantial gains for classes where street-level views are informative.
2. We systematically evaluate four masking strategies for isolating the target building and show that an RGB-M approach, appending the binary footprint mask as a fourth channel, provides the best trade-off between spatial focus and contextual information.
3. We construct a multi-modal building inspection dataset of 32,135 buildings (61,672 segments) across ten countries, pairing satellite imagery with variable numbers of street-level views and building footprint masks.
4. We compare two backbones (ResNet-50, DINOv2-S) and multiple fine-tuning strategies, demonstrating that fully fine-tuned DINOv2-S consistently outperforms the convolutional baseline on both modalities.

## 2. Related Work

**Satellite imagery for building analysis.** CNN-based methods have been widely applied to satellite imagery for building footprint extraction [16, 17, 38], damage detection [36], and roof type identification [19]. Vision Transformers have since improved large-scale building extraction [33] and damage assessment [18] through their ability to capture global spatial context. More recently, self-supervised foundation models such as DINOv2 [26] have demonstrated strong transfer to remote sensing tasks, particularly in low-label regimes [24, 28]. Despite these advances, relying solely on satellite imagery limits inspection to attributes visible from above, missing facade-level detail that is critical for comprehensive building assessment.

**Street-level imagery for building analysis.** Street-level images offer ground-level perspectives on facades, materials, and structural elements that are occluded in satellite views. Deep learning approaches have been applied to building typology classification [7, 21, 31], property value

estimation [37], facade parsing [20, 32], and floor count estimation [13]. Semi-supervised approaches combine street-level imagery with auxiliary data such as OpenStreetMap metadata for building height estimation [23]. Biljecki and Ito [1] provide a comprehensive survey of street-view imagery in urban analytics. Key challenges include variable lighting and weather conditions, occlusion by vegetation and vehicles, inconsistent camera calibration across regions, and privacy-related blurring [10].

**Fusion of satellite and street-level modalities.** Combining satellite and street-level data leverages their complementary strengths: broad spatial coverage from above and detailed facade information from ground level. This multi-modal approach has improved performance in house price estimation [22], land use classification [2, 29], building type classification [11], socioeconomic prediction [30], and flood risk assessment [35]. Early fusion methods concatenate or sum global feature vectors, treating modalities symmetrically without exploiting their complementary spatial structure [6]. Recent attention-based approaches process multiple views with learned weighting, focusing on the most informative inputs [3, 8, 12]. However, most existing methods operate on a fixed number of views per building, discarding spatial token-level detail through global pooling before fusion.

Our work differs in three respects. First, we fuse at the *spatial token level* rather than the feature vector level, preserving fine-grained patch information from both modalities. Second, we employ Perceiver IO [15] to compress a variable-length token sequence into a fixed-size latent representation through cross-attention, naturally handling buildings with any number of street-level views. Third, we build on a self-supervised DINOv2 backbone rather than task-specific supervised features, providing richer representations for both modalities.

## 3. Method

We describe the dataset construction (Sec. 3.1), masking strategies for isolating the target building (Sec. 3.2), unimodal baselines (Sec. 3.3), and the Perceiver IO fusion architecture (Sec. 3.4).

### 3.1. Dataset

We construct a multi-modal dataset of 32,135 buildings (61,672 segments) across ten countries, with the Netherlands (17,632), UK (10,872), and France (1,374) contributing the largest shares. Labels are assigned at the roof segment level, where each building may contain multiple roof segments. The dataset supports two multi-label classification tasks: **roof elements** (6 classes: solar panels, dormer, skylight, roof window, chimney, external installations) and

Table 1. Label distribution at segment level. Both tasks exhibit strong class imbalance.

Task	Label	Count
Roof Elements	Solar Panels	6,905
	Dormer	4,210
	Skylight	999
	Roof Window	10,726
	Chimney	19,155
	External Installations	2,064
Roof Materials	Bitumen	27,293
	Slate	6,932
	Tiles	23,874
	Aluminium	2,693
	Thatch	184
	Corrugated Sheets	1,811
	Glass	280

**roof materials** (7 classes: bitumen, slate, tiles, aluminium, thatch, corrugated sheets, glass). Class distributions are heavily imbalanced (Tab. 1), with chimney (19,155 segments) and bitumen (27,293) being the most frequent, while thatch (184) and glass (280) are extremely rare. Figure 2 shows the geographic distribution of the dataset.

**Satellite imagery.** For each segment, a single satellite image is cropped to a fixed 42×42 m physical area centered on the building. Sources include Google Maps and higher-resolution national aerial imagery (e.g., PDOK in the Netherlands). Building footprints are obtained from OpenStreetMap [25] or the Dutch BAG cadastral registry (Fig. 4).

**Street-level imagery.** Street-level views are sourced from Google Street View and, in the Netherlands, from Cyclomedia panoramas. A custom selection algorithm maximizes facade visibility while minimizing redundancy, yielding an average of 4.54 images per segment (280,150 image-mask pairs total). For each image, a pixel-level mask is generated by projecting the building footprint into the camera view using the footprint polygon, camera position, and an estimated building height. Images with less than 20% building visibility (as assessed by a SegFormer-B0 [34] trained on Cityscapes [4]) are discarded, removing 22% of image-mask pairs. During training and inference, up to 8 street-level images are sampled per segment (Figs. 3, 5 and 6).

**Splits.** The dataset is split 85%/7.5%/7.5% at the segment level into train, validation, and test sets.

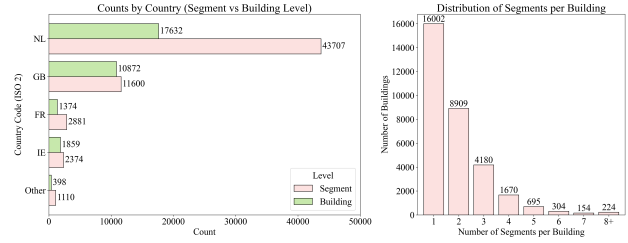


Figure 2. Dataset statistics: building and segment counts by country (left) and distribution of segments per building (right). The Netherlands contributes the largest share.

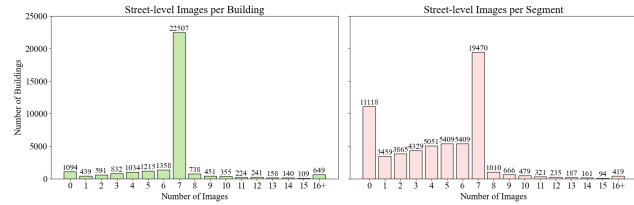


Figure 3. Distribution of street-level images per building (left) and per segment (right). Most buildings have 7 images; at the segment level, many segments have 0 or 7 images.



Figure 4. Satellite imagery challenges: no issues, low resolution, misaligned footprint, wrong footprint, and occlusion by trees/shadows. Showing image and building mask.



Figure 5. Street-level imagery challenges: no issues, occlusion by vehicles/vegetation, privacy blurring, camera location offset, and building height error affecting mask projection.



Figure 6. Examples of street-level occlusion patterns. Vegetation, vehicles, and neighboring structures partially obscure the target building.

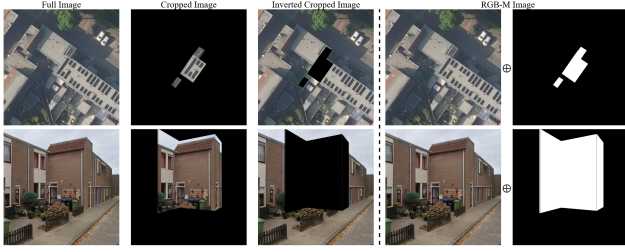


Figure 7. Four masking strategies applied to satellite (top) and street-level (bottom) imagery. From left to right: full image, cropped (background zeroed), inverted crop (building zeroed), and RGB-M (mask appended as 4th channel).

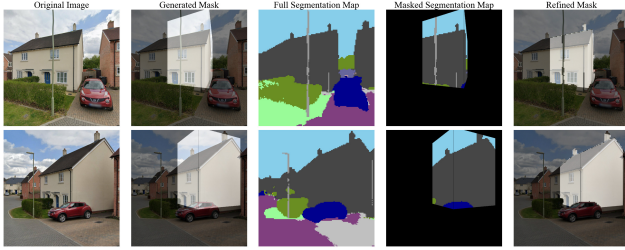


Figure 8. Street-level mask generation pipeline. From left to right: original image, projected building footprint mask, full semantic segmentation map (SegFormer-B0), masked segmentation, and refined mask.

### 3.2. Masking Strategies

To isolate the target building in each image, we evaluate four masking strategies (Fig. 7) using the binary building footprint mask  $M$ :

1. **Full image:** The unmodified RGB image ( $\mathbb{R}^{H \times W \times 3}$ ).
2. **Crop:** Element-wise product  $I_{\text{rgb}} \odot M$ , zeroing out all pixels outside the building footprint.
3. **Inverted crop:**  $I_{\text{rgb}} \odot (1 - M)$ , retaining only the surrounding context as a sanity check.
4. **RGB-M:** The mask is appended as a fourth input channel,  $[I_{\text{rgb}}; M] \in \mathbb{R}^{H \times W \times 4}$ , letting the model learn to balance building focus with contextual information.

For street-level imagery, pixel-level masks are generated by projecting the building footprint into the camera view. Figure 8 illustrates the mask generation pipeline, and Fig. 9 shows a limitation of the refinement step where sparse vegetation causes relevant building areas to be excluded.

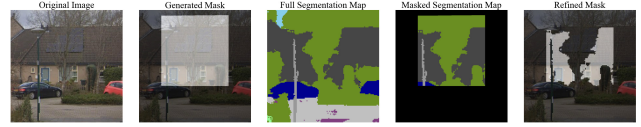


Figure 9. Mask refinement limitation: sparse vegetation in the segmentation map causes relevant building areas to be incorrectly excluded from the refined mask.

### 3.3. Uni-modal Models

**Backbone.** We compare ResNet-50 [9] and DINOv2-S [26]. For ResNet-50, a global average-pooled feature vector serves as the building representation. For DINOv2-S, we use the [CLS] token output. Both feed into task-specific linear classifier heads for roof elements and roof materials. For the RGB-M masking strategy, the first convolutional layer (ResNet-50) or patch embedding projection (DINOv2-S) is adapted to accept 4-channel input.

**Satellite model.** A single satellite image is encoded into a global feature vector and passed to both classifier heads (Fig. 10). Since each building has exactly one satellite view, no aggregation is needed; the backbone output directly serves as the building-level representation.

**Street-level model.** Each street-level image is independently encoded by the same backbone (Fig. 11). The resulting feature vectors are aggregated via max pooling across views and passed to the classifiers. We also evaluate mean pooling and attention-based pooling [14]; max pooling performs best overall.

### 3.4. Multi-modal Fusion

We evaluate three fusion strategies of increasing complexity, all using DINOv2-S with RGB-M masking.

**Concatenation.** The satellite feature vector and the max-pooled street-level feature vector are concatenated and passed to the classifiers (Fig. 12). When no street-level images are available, a learnable placeholder vector is substituted. This baseline has zero additional fusion parameters.

**Feature Vector Transformer.** Feature vectors from the satellite image and each individual street-level view are combined into a single sequence (Fig. 13), augmented with a learnable [CLS] token and modality embeddings. A standard transformer encoder with  $L$  layers and  $h=8$  attention heads processes this sequence; the [CLS] output is used for classification. This eliminates the need for explicit pooling and handles variable input counts.

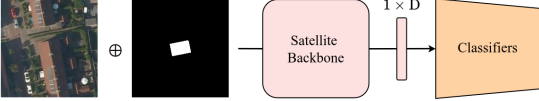


Figure 10. Uni-modal satellite model. The RGB-M input (4 channels) is encoded by the backbone into a  $1 \times D$  feature vector and passed to task-specific classifiers.

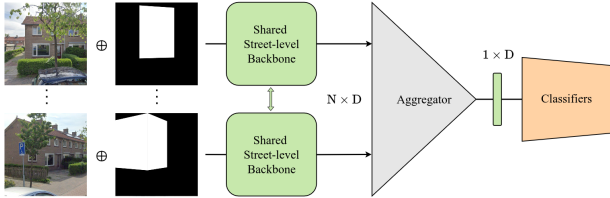


Figure 11. Uni-modal street-level model. Each street-level image is independently encoded by a shared backbone. Feature vectors are aggregated (max/mean/attention pooling) into a single representation for classification.

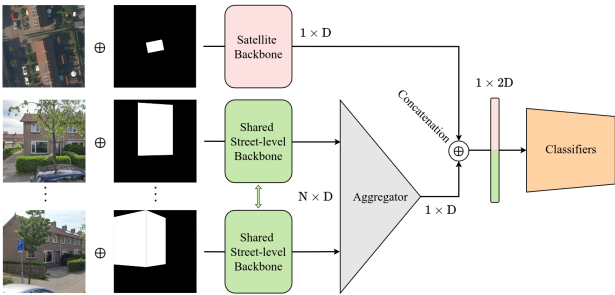


Figure 12. Concatenation fusion baseline. Satellite and aggregated street-level feature vectors are concatenated and passed to classifiers. Zero additional fusion parameters.

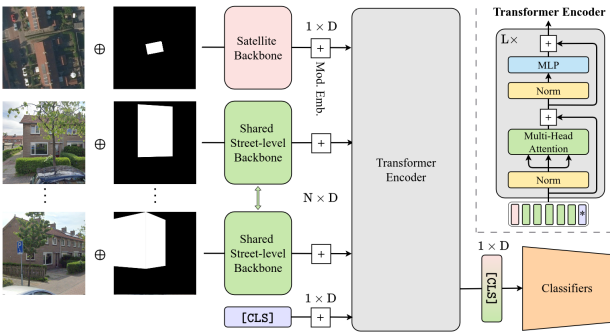


Figure 13. Feature Vector Transformer fusion. Individual feature vectors from all views are combined with a learnable [CLS] token and modality embeddings, then processed by a transformer encoder.

**Perceiver IO.** Our main contribution (Fig. 14) operates on *spatial tokens* rather than pooled feature vectors, preserving fine-grained patch-level detail. Given a satellite image and  $N$  street-level images, each processed by the DINOv2-S backbone into  $P$  patch tokens of dimension  $D$ , the full input sequence is  $X \in \mathbb{R}^{(N+1)P \times D}$ . Each token is augmented with three learned embeddings: (i) a 2D positional embedding encoding its spatial location within the source image, (ii) a modality embedding distinguishing satellite from street-level tokens, and (iii) a view embedding for inter-view localization.

The Perceiver IO processes this variable-length input in three stages:

1. **Cross-attention encoder.** A single-head cross-attention layer compresses  $X$  into a fixed-size latent array  $Z_0 \in \mathbb{R}^{N_z \times D_z}$  using a learnable query array, where  $N_z \ll (N+1)P$ .
2. **Latent refinement.**  $B$  blocks of  $L$  self-attention sub-layers (with parameters shared across blocks but not within) refine the latent representation.
3. **Cross-attention decoder.** A single-head cross-attention layer with a learnable output query  $q \in \mathbb{R}^{1 \times D_z}$  attends over the refined latents to produce a global embedding  $y \in \mathbb{R}^{D_{out}}$ , which is passed to the classifier heads.

This architecture compresses an arbitrarily long token sequence into a fixed-size bottleneck, naturally handling any number of street-level views without padding or truncation.

### 3.5. Training

The total loss is  $\mathcal{L} = 0.5 \cdot \mathcal{L}_{RE} + 0.5 \cdot \mathcal{L}_{RM}$ , where  $\mathcal{L}_{RE}$  and  $\mathcal{L}_{RM}$  are binary cross-entropy losses for roof elements and roof materials respectively. We use AdamW with weight decay 0.05, separate learning rates for the backbone ( $5 \times 10^{-5}$ ) and fusion heads ( $5 \times 10^{-4}$ ), linear warm-up (5 iterations) followed by cosine annealing ( $T_{max}=50$ ), and early stopping with patience 8. Data augmentation includes random horizontal flips, rotations (up to  $180^\circ$  for satellite,  $8^\circ$  for street-level), brightness/contrast jitter, color jitter, and Gaussian blur for satellite images; street-level images receive a lighter subset given their natural variability. Images are resized to  $518 \times 518$  pixels (DINOv2-S’s native resolution). Training uses mixed-precision (float16) on  $2 \times$  NVIDIA RTX 3090 GPUs with batch size 32 for the Perceiver IO model. A custom dataloader buckets samples by street-level image count, avoiding padding overhead.

## 4. Experiments

We evaluate along four axes: (1) masking strategies, (2) backbone and fine-tuning, (3) input resolution, and (4) fusion architecture. All results are reported as macro-averaged mean Average Precision (mAP) over classes. For roof materials, we additionally report mAP\*, computed

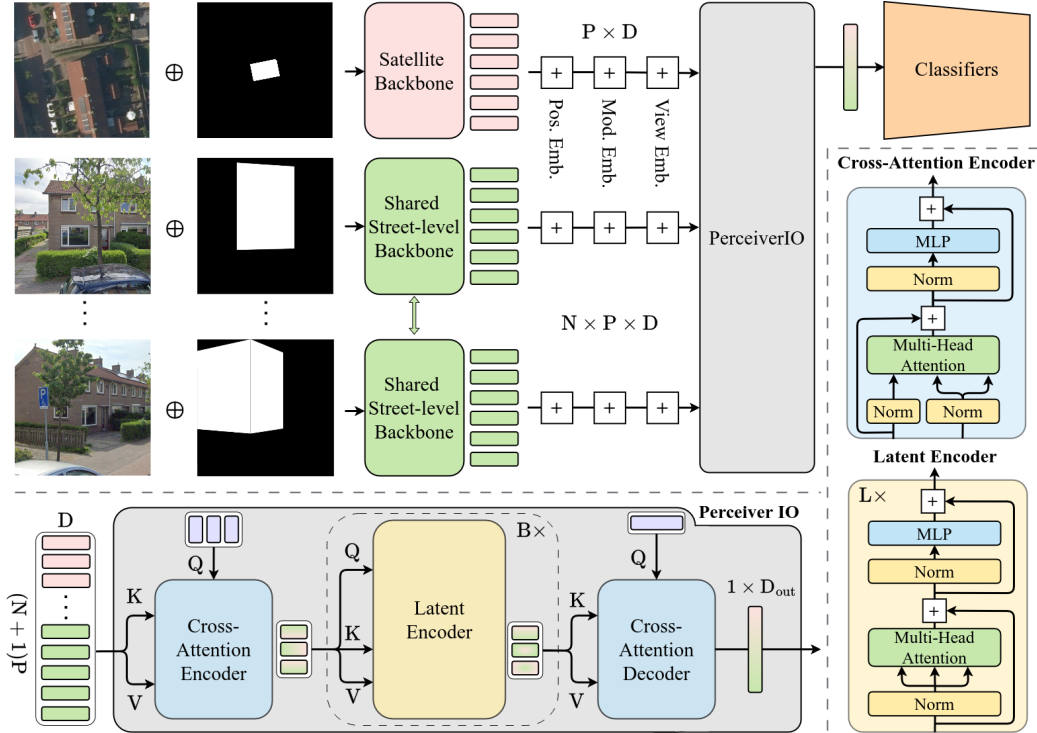


Figure 14. Perceiver IO fusion architecture. A satellite image and  $N$  street-level images are encoded by shared DINOv2 backbones into spatial patch tokens, augmented with positional, modality, and view embeddings. The cross-attention encoder compresses the variable-length token sequence into a fixed-size latent array. After refinement through  $B$  blocks of self-attention layers, a cross-attention decoder produces a global embedding for classification.

Table 2. Satellite masking strategies. Best per backbone in **bold**.

Backbone	Masking	Elem	Mat	Mat*
ResNet-50	Full	0.867	0.694	0.754
	Crop	<b>0.928</b>	0.701	0.743
	Inv-Crop	0.650	0.502	0.649
	RGB-M	0.924	<b>0.721</b>	<b>0.769</b>
DINOv2-S	Full	0.891	<b>0.736</b>	<b>0.788</b>
	Crop	0.927	0.688	0.733
	Inv-Crop	0.696	0.621	0.724
	RGB-M	<b>0.939</b>	0.729	<b>0.788</b>

Table 3. Street-level masking strategies. Best in **bold**.

Backbone	Masking	Elem	Mat	Mat*
ResNet-50	Full	0.596	0.526	0.613
	Crop	<b>0.684</b>	<b>0.554</b>	<b>0.660</b>
	Inv-Crop	0.595	0.507	0.608
	RGB-M	0.626	0.546	0.639
DINOv2-S	Full	0.635	0.551	0.648
	Crop	0.666	0.558	0.666
	Inv-Crop	0.639	0.563	0.644
	RGB-M	<b>0.712</b>	<b>0.597</b>	<b>0.687</b>

over a reliable subset of five classes that excludes thatch and glass, which have very few training samples (184 and 280 respectively).

#### 4.1. Masking Strategies

Tables 2 and 3 compare the four masking strategies on satellite and street-level imagery, respectively. Across both modalities, DINOv2-S with RGB-M masking achieves the best overall performance: 0.939 mAP for roof elements and 0.729 for roof materials on satellite, 0.712 and 0.597 on street-level. The RGB-M strategy consistently outperforms

alternatives for DINOv2-S by providing the building footprint as a soft spatial prior without discarding contextual information. Hard cropping is competitive for ResNet-50 on satellite (0.928 mAP for roof elements) but degrades more for DINOv2-S, likely because the zero-padded background conflicts with DINOv2’s pretrained patch statistics. The inverted-crop sanity check confirms that surrounding context alone carries meaningful signal (0.696 mAP for roof elements on DINOv2-S satellite), but performance is substantially lower than mask-inclusive strategies.

Grad-CAM visualizations confirm these findings qualita-

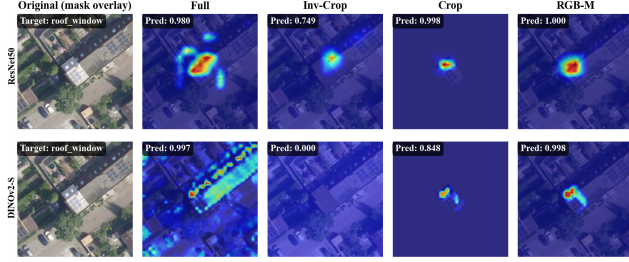


Figure 15. Grad-CAM visualizations for satellite masking strategies (ResNet-50 top, DINOv2-S bottom). Full image attention is diffuse; Crop forces focus onto the building; Inv-Crop attends to context only.

tively (Figs. 15 and 16). Without masking, attention is diffusely spread across the entire scene. Hard cropping forces the model to focus exclusively on the building footprint, while the inverted crop attends only to context. RGB-M produces the most balanced activation pattern: the model attends primarily to the building while retaining access to contextual cues at the boundary, consistent with its superior quantitative performance.

We also compared the standard footprint-projected masks against refined masks produced by the SegFormer-B0 segmentation model, with and without the 20% visibility threshold. The standard mask consistently outperforms the refined version, suggesting that segmentation-based refinement can remove useful building regions (e.g., behind sparse vegetation) without compensating gains. Applying the visibility threshold has little effect with standard masks, indicating that the model is reasonably robust to partially occluded views.

## 4.2. Backbone and Fine-tuning

Table 4 shows that full fine-tuning of DINOv2-S yields the highest mAP for both tasks, with a large gap over linear probing (+22.4 mAP for roof elements, +18.1 mAP for roof materials). Partial strategies (last-3 layers, progressive unfreezing) close most of the gap but fall short of full adaptation, suggesting the domain shift from natural images to aerial/street-level building imagery requires updating early feature layers. The same pattern holds for street-level imagery, where full fine-tuning achieves 0.703 mAP for roof elements vs. 0.591 for linear probing.

## 4.3. Input Resolution

Performance peaks at  $518 \times 518$  (Tab. 5), which matches DINOv2-S’s pretraining resolution. Higher resolution (784) does not help, likely because the interpolated positional embeddings introduce artifacts. In contrast, ResNet-50 benefits from higher resolution up to 784, consistent with its lack of resolution-dependent positional priors.

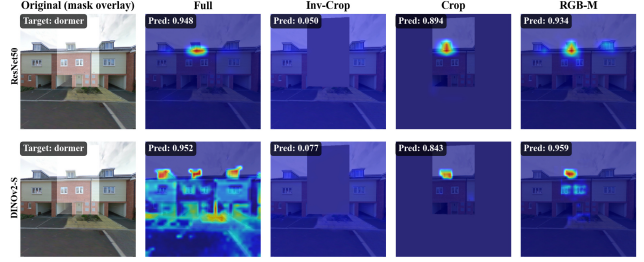


Figure 16. Grad-CAM visualizations for street-level masking strategies (ResNet-50 top, DINOv2-S bottom). Without masking, attention is spread; Crop isolates the building facade.

Table 4. DINOv2-S fine-tuning strategies on satellite imagery with RGB-M masking.

Strategy	Elem	Mat	Mat*
Linear probing	0.715	0.548	0.651
Last-3 layers	0.912	0.724	0.784
Progressive	0.912	0.725	0.792
Full	<b>0.939</b>	<b>0.729</b>	0.786

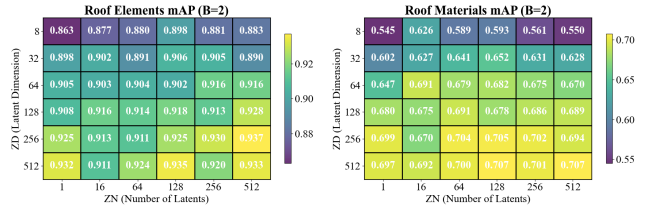


Figure 17. Perceiver IO sensitivity to latent configuration ( $B=2$ ). mAP for roof elements (left) and materials (right) as a function of the number of latents  $N_z$  and latent dimensionality  $D_z$ . Performance depends primarily on  $D_z$ ; even  $N_z=1$  suffices at high dimensionality.

## 4.4. Fusion Architectures

**Perceiver IO configuration.** Figure 17 shows the sensitivity to latent configuration. We sweep over the number of latent vectors  $N_z \in \{1, 16, 64, 128, 256, 512\}$ , latent dimensionality  $D_z \in \{8, 32, 64, 128, 256, 512\}$ , and refinement blocks  $B \in \{0, 1, 2, 4\}$ . Latent dimensionality has a much stronger impact than the number of latents; even  $N_z=1$  achieves near-peak performance with  $D_z=512$ . We select  $N_z=128$ ,  $D_z=512$ ,  $B=2$  for final experiments as the best trade-off.

Table 6 presents the overall comparison. The satellite-only model achieves the highest macro-averaged mAP, with Perceiver IO as the best fusion method (0.935 for elements, 0.707 for materials). However, macro mAP obscures important per-class differences. Table 7 reveals that the Perceiver IO model substantially improves on classes where street-level imagery provides complementary information: slate

Table 5. Impact of input resolution on DINOv2-S satellite performance (RGB-M masking).

Resolution	Elem	Mat
$224 \times 224$	0.904	0.710
$336 \times 336$	0.924	0.711
$518 \times 518$	<b>0.939</b>	<b>0.729</b>
$784 \times 784$	0.928	0.721

Table 6. Overall model comparison. All models use DINOv2-S with RGB-M masking. Best overall in **bold**; best fusion model underlined.

Model	Params	Elem	Mat	Mat*
Satellite only	–	<b>0.939</b>	<b>0.729</b>	<b>0.786</b>
Street-level only	–	0.712	0.597	0.687
Concatenation	0M	0.912	0.714	0.782
FV Transformer	13.0M	0.927	0.705	0.767
Perceiver IO	25.7M	<u>0.935</u>	<u>0.707</u>	<u>0.774</u>

gains +11.3 AP ( $0.778 \rightarrow 0.891$ ), dormer +1.3 AP, tiles +1.0 AP, roof window +0.9 AP, and glass +4.5 AP. In contrast, the satellite-only model retains an advantage for classes that are primarily visible from above: skylight, external installations, bitumen, aluminium, thatch, and corrugated sheets. For these classes, street-level views introduce noise rather than useful signal, as the relevant features are occluded or absent at ground level.

The concatenation baseline (0.912 mAP for roof elements) underperforms both the satellite-only model and the Perceiver IO, indicating that naive feature-level fusion degrades the satellite signal. The Feature Vector Transformer (0.927 mAP for roof elements) improves over concatenation but still loses spatial detail through global pooling before fusion; sweeping the number of encoder layers ( $L \in \{1, 2, 4, 6\}$ ) shows that  $L=1$  performs comparably to deeper configurations, so the additional capacity provides little benefit at the feature-vector level. Perceiver IO’s token-level fusion recovers much of this lost information.

## 5. Discussion

**When does fusion help?** The per-class analysis in Tab. 7 reveals a clear pattern: fusion improves classification for attributes that are visible and distinctive in street-level imagery. Slate and tiles, for example, are visually similar from above but readily distinguishable at ground level through texture and color differences, explaining the +11.3 AP gain for slate. Dormers and roof windows protrude from the roof plane and are often visible from the street, yielding consistent improvements. In contrast, skylights, external installations, and bitumen roofing are best observed from above, and adding street-level tokens for these classes dilutes the satellite signal.

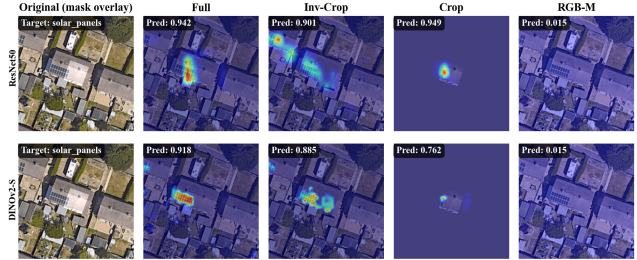


Figure 18. Grad-CAM visualizations for satellite imagery across masking strategies (ResNet-50 top, DINOv2-S bottom). RGB-M focuses attention on the target building while retaining contextual awareness. Hard cropping forces attention onto the masked region but removes useful context.

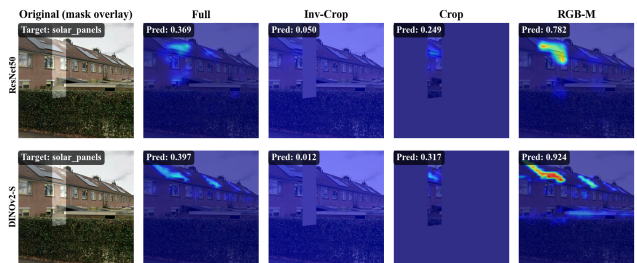


Figure 19. Grad-CAM visualizations for street-level imagery with RGB-M masking (ResNet-50 top, DINOv2-S bottom). RGB-M effectively focuses attention on the target building facade even in cluttered street scenes.

**RGB-M as a soft spatial prior.** The RGB-M masking strategy outperforms hard cropping because it provides the building footprint as an additional input channel rather than destructively zeroing out context pixels. This is especially important for DINOv2-S, whose pretrained patch statistics assume complete image patches. Hard cropping introduces zero-filled patches that fall outside the pretraining distribution, degrading feature quality. The inverted-crop experiment confirms that context alone carries meaningful signal—nearby buildings, street patterns, and vegetation provide cues about the target building’s type and materials. Figures 18 and 19 illustrate this effect for both satellite and street-level imagery.

**DINOv2 vs. ResNet-50.** Fully fine-tuned DINOv2-S consistently outperforms ResNet-50 despite having a similar parameter count. The gap is largest for roof materials (+0.8 mAP on satellite), suggesting that DINOv2’s self-supervised pretraining produces features that better capture fine-grained material textures. Linear probing performs poorly (0.715 mAP for roof elements), indicating that the domain gap between natural images and building inspection imagery requires substantial feature adaptation.

Table 7. Per-class Average Precision for the satellite-only baseline and Perceiver IO fusion model. Classes where fusion improves by  $\geq 1$  AP point are highlighted in **bold**.

Model	Roof Elements						Roof Materials						
	Solar	Dorm	Sky	Win	Chim	Ext	Bit	Slate	Tiles	Alu	Thatch	Corr	Glass
Satellite only	0.979	0.932	<b>0.882</b>	0.971	0.976	<b>0.892</b>	<b>0.961</b>	0.778	0.946	<b>0.637</b>	<b>0.876</b>	<b>0.609</b>	0.294
Perceiver IO	0.981	<b>0.945</b>	0.858	<b>0.980</b>	0.978	0.867	0.944	<b>0.891</b>	<b>0.956</b>	0.591	0.741	0.490	<b>0.339</b>
$\Delta$	+0.2	+1.3	-2.4	+0.9	+0.2	-2.5	-1.7	+11.3	+1.0	-4.6	-13.5	-11.9	+4.5

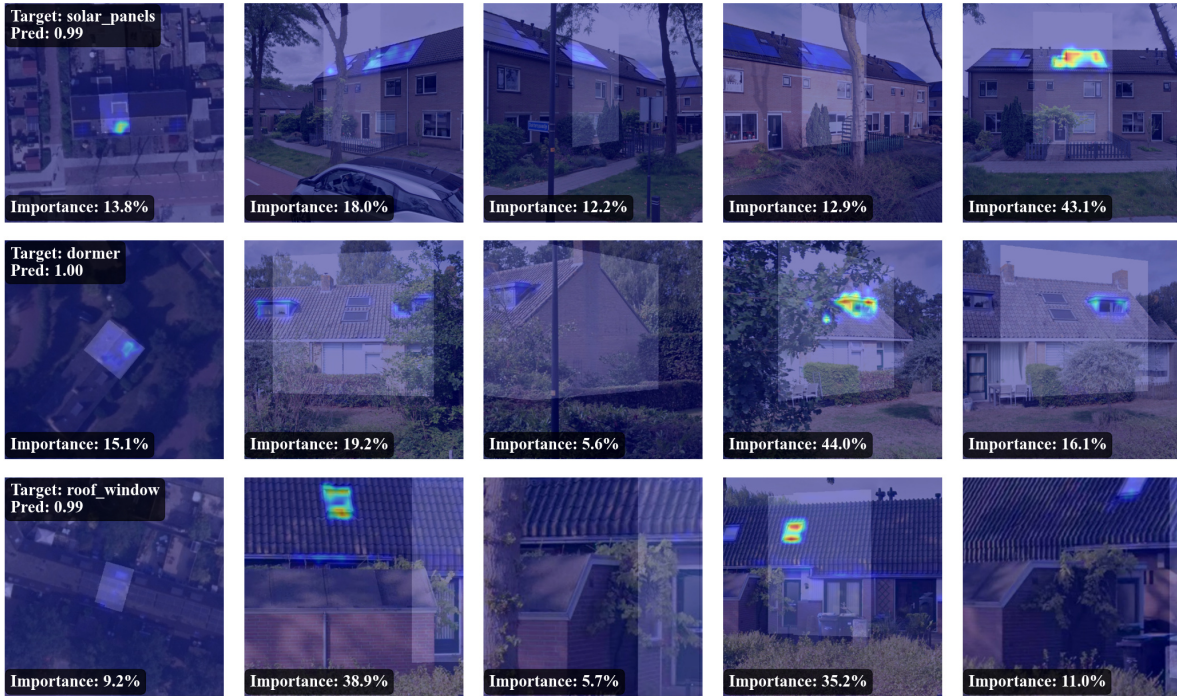


Figure 20. Perceiver IO attention rollout visualizations for three buildings. Each row shows the satellite image (left, with attention overlay) and street-level views with per-view importance scores. The model correctly localizes solar panels (top), dormers (middle), and roof windows (bottom) across modalities, assigning higher importance to views where the target attribute is visible.

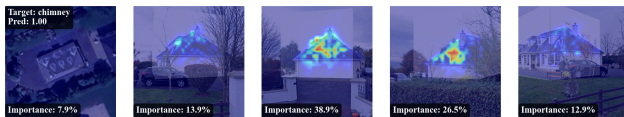


Figure 21. Perceiver IO attention rollout for chimney detection—a failure case. Attention is diffusely spread across views without clear localization, suggesting the model may rely on contextual shortcuts rather than localizing the chimney directly.

**Perceiver IO design choices.** Latent dimensionality ( $D_z$ ) matters more than the number of latents ( $N_z$ ): reducing  $D_z$  from 512 to 64 degrades performance substantially, while  $N_z=1$  with  $D_z=512$  achieves near-peak results. This suggests that the cross-attention bottleneck must preserve sufficient representational capacity per latent, but the model can

compress all spatial tokens into very few latent vectors without losing critical information. Adding refinement blocks ( $B=2$ ) improves mAP for roof elements but slightly hurts mAP for roof materials; deeper refinement ( $B=4$ ) degrades both tasks, likely due to over-smoothing. Attention rollout visualizations (Fig. 20) confirm that the model localizes target attributes across modalities, though for frequent classes like chimney, attention is diffuse (Fig. 21), suggesting reliance on contextual shortcuts.

**Limitations.** The satellite-only model’s higher macro mAP reflects a fundamental asymmetry: all 13 target classes are at least partially visible from above, but only a subset are informative from ground level. Street-level imagery also suffers from inconsistent coverage—some buildings have many high-quality views while others have



Figure 22. Challenging classes: Aluminium (top), Corrugated Sheets (middle), Glass (bottom). Left columns show top-3 correct predictions; right columns show top-3 incorrect predictions. These classes suffer from small sample sizes and confusion with visually similar materials.

none—and from noise sources including occlusion, privacy blurring, and camera positioning errors. Class imbalance (thatch: 184 samples, glass: 280) limits reliable evaluation for rare classes, and visually similar materials such as aluminium and corrugated sheets remain challenging regardless of the model (Fig. 22).

## 6. Conclusion

We presented a Perceiver IO-based architecture for multi-modal building inspection that fuses satellite and street-level imagery at the spatial token level using a shared DINOv2 backbone. Systematic experiments on a 32,135-building dataset across ten countries yield three main findings. First, appending the building footprint mask as a fourth input channel (RGB-M) provides the most effective strategy for isolating the target building, outperforming hard cropping and full-image baselines. Second, fully fine-tuned DINOv2-S consistently outperforms ResNet-50 on both modalities, even on this domain-specific dataset. Third, Perceiver IO fusion delivers substantial per-class improvements for attributes visible from street level (+11.3 AP for slate, +4.5 AP for glass, +1.3 AP for dormers), though the satellite-only baseline retains higher macro-averaged mAP due to classes that are only visible from above.

These results demonstrate that multi-modal fusion is most valuable when the modalities provide genuinely complementary views. Future work includes encoding street-level camera metadata (GPS coordinates, viewing angle, distance) as geometric positional embeddings to improve cross-view reasoning; exploiting the token-based architecture for patch-level masking, down-weighting or removing patches outside the building region for harder spatial attention than RGB-M; and multi-task learning that jointly performs classification, segmentation, and regression (e.g., building height, floor count) to encourage richer shared representations.

## References

- [1] Filip Biljecki and Koichi Ito. Street view imagery in urban analytics and gis: A review. *Landscape and Urban Planning*, 215:104217, 2021. 2
- [2] Rui Cao, Jiasong Zhu, Wei Tu, Qingquan Li, Jinzhou Cao, Bozhi Liu, Qian Zhang, and Guoping Qiu. Integrating aerial and street view images for urban land use classification. *Remote Sensing*, 10(10):1553, 2018. 1, 2
- [3] Boan Chen, Quanlong Feng, Bowen Niu, Fengqin Yan, Bingbo Gao, Jianyu Yang, Jianhua Gong, and Jiantao Liu. Multi-modal fusion of satellite and street-view images for urban village classification based on a dual-branch deep neural network. *International Journal of Applied Earth Observation and Geoinformation*, 109:102794, 2022. 2
- [4] Marius Cordts, Mohamed Omran, Sebastian Ramos, Timo Rehfeld, Markus Enzweiler, Rodrigo Benenson, Uwe Franke, Stefan Roth, and Bernt Schiele. The cityscapes dataset for semantic urban scene understanding. In *Proceedings of the IEEE conference on computer vision and pattern recognition*, pages 3213–3223, 2016. 3
- [5] European Commission. Energy performance of buildings directive. [https://energy.ec.europa.eu/topics/energy-efficiency/energy-efficient-buildings/energy-performance-buildings-directive\\_en](https://energy.ec.europa.eu/topics/energy-efficiency/energy-efficient-buildings/energy-performance-buildings-directive_en), 2024. 1
- [6] Runyu Fan, Jun Li, Fengpeng Li, Wei Han, and Lizhe Wang. Multilevel spatial-channel feature fusion network for urban village classification by fusing satellite and streetview images. *IEEE Transactions on Geoscience and Remote Sensing*, 60:1–13, 2022. 2
- [7] Daniela Gonzalez, Diego Rueda-Plata, Ana B Acevedo, Juan C Duque, Raúl Ramos-Pollán, Alejandro Betancourt, and Sebastian García. Automatic detection of building typology using deep learning methods on street level images. *Building and Environment*, 177:106805, 2020. 2
- [8] Wentong Guo, Cheng Xu, and Sheng Jin. Fusion of satellite and street view data for urban traffic accident hotspot identification. *International Journal of Applied Earth Observation and Geoinformation*, 130:103853, 2024. 2
- [9] Kaiming He, Xiangyu Zhang, Shaoqing Ren, and Jian Sun. Deep residual learning for image recognition. In *Proceedings of the IEEE conference on computer vision and pattern recognition*, pages 770–778, 2016. 4
- [10] Nan He and Guanghao Li. Urban neighbourhood environment assessment based on street view image processing: A review of research trends. *Environmental Challenges*, 4: 100090, 2021. 1, 2
- [11] Eike Jens Hoffmann, Yuanyuan Wang, Martin Werner, Jian Kang, and Xiao Xiang Zhu. Model fusion for building type classification from aerial and street view images. *Remote Sensing*, 11(11):1259, 2019. 1, 2
- [12] Yingjing Huang, Fan Zhang, Yong Gao, Wei Tu, Fabio Duarte, Carlo Ratti, Diansheng Guo, and Yu Liu. Comprehensive urban space representation with varying numbers of street-level images. *Computers, Environment and Urban Systems*, 106:102043, 2023. 2

- [13] Gianni Cristian Iannelli and Fabio Dell’Acqua. Extensive exposure mapping in urban areas through deep analysis of street-level pictures for floor count determination. *Urban Science*, 1(2):16, 2017. 2
- [14] Maximilian Ilse, Jakub Tomczak, and Max Welling. Attention-based deep multiple instance learning. In *International conference on machine learning*, pages 2127–2136. PMLR, 2018. 4
- [15] Andrew Jaegle, Sebastian Borgeaud, Jean-Baptiste Alayrac, Carl Doersch, Catalin Ionescu, David Ding, Skanda Koppala, Daniel Zoran, Andrew Brock, Evan Shelhamer, et al. Perceiver io: A general architecture for structured inputs & outputs. *arXiv preprint arXiv:2107.14795*, 2021. 2
- [16] Shunping Ji, Shiqing Wei, and Meng Lu. Fully convolutional networks for multisource building extraction from an open aerial and satellite imagery data set. *IEEE Transactions on geoscience and remote sensing*, 57(1):574–586, 2018. 2
- [17] Shunping Ji, Shiqing Wei, and Meng Lu. A scale robust convolutional neural network for automatic building extraction from aerial and satellite imagery. *International journal of remote sensing*, 40(9):3308–3322, 2019. 2
- [18] Navjot Kaur, Cheng-Chun Lee, Ali Mostafavi, and Ali Mahdavi-Amiri. Large-scale building damage assessment using a novel hierarchical transformer architecture on satellite images. *Computer-Aided Civil and Infrastructure Engineering*, 38(15):2072–2091, 2023. 2
- [19] Jonguk Kim, Hyansu Bae, Hyunwoo Kang, and Suk Gyu Lee. Cnn algorithm for roof detection and material classification in satellite images. *Electronics*, 10(13):1592, 2021. 2
- [20] Gefei Kong and Hongchao Fan. Enhanced facade parsing for street-level images using convolutional neural networks. *IEEE Transactions on Geoscience and Remote Sensing*, 59(12):10519–10531, 2020. 2
- [21] Dominik Laupheimer, Patrick Tutzauer, Norbert Haala, and Marc Spicker. Neural networks for the classification of building use from street-view imagery. *ISPRS Annals of the Photogrammetry, Remote Sensing and Spatial Information Sciences*, 4:177–184, 2018. 2
- [22] Stephen Law, Brooks Paige, and Chris Russell. Take a look around: using street view and satellite images to estimate house prices. *ACM Transactions on Intelligent Systems and Technology (TIST)*, 10(5):1–19, 2019. 1, 2
- [23] Hao Li, Zhendong Yuan, Gabriel Dax, Gefei Kong, Hongchao Fan, Alexander Zipf, and Martin Werner. Semi-supervised learning from street-view images and openstreetmap for automatic building height estimation. *arXiv preprint arXiv:2307.02574*, 2023. 2
- [24] Siqi Lu, Junlin Guo, James R Zimmer-Dauphinee, Jordan M Nieusma, Xiao Wang, Steven A Wernke, Yuankai Huo, et al. Vision foundation models in remote sensing: A survey. *IEEE Geoscience and Remote Sensing Magazine*, 2025. 2
- [25] OpenStreetMap contributors. Planet dump retrieved from <https://planet.osm.org>. <https://www.openstreetmap.org>, 2025. 3
- [26] Maxime Oquab, Timothée Darcet, Théo Moutakanni, Huy Vo, Marc Szafranec, Vasil Khalidov, Pierre Fernandez, Daniel Haziza, Francisco Massa, Alaaeldin El-Nouby, et al. Dinov2: Learning robust visual features without supervision. *arXiv preprint arXiv:2304.07193*, 2023. 2, 4
- [27] Andrew G Rundle, Michael DM Bader, Catherine A Richards, Kathryn M Neckerman, and Julien O Teitler. Using google street view to audit neighborhood environments. *American journal of preventive medicine*, 40(1):94–100, 2011. 1
- [28] Linus Scheibenreif, Joëlle Hanna, Michael Mommert, and Damian Borth. Self-supervised vision transformers for land-cover segmentation and classification. In *Proceedings of the IEEE/CVF Conference on Computer Vision and Pattern Recognition*, pages 1422–1431, 2022. 2
- [29] Shivangi Srivastava, John E Vargas-Munoz, and Devis Tuia. Understanding urban landuse from the above and ground perspectives: A deep learning, multimodal solution. *Remote sensing of environment*, 228:129–143, 2019. 2
- [30] Esra Suel, Samir Bhatt, Michael Brauer, Seth Flaxman, and Majid Ezzati. Multimodal deep learning from satellite and street-level imagery for measuring income, overcrowding, and environmental deprivation in urban areas. *Remote Sensing of Environment*, 257:112339, 2021. 2
- [31] Salma Taoufiq, Balázs Nagy, and Csaba Benedek. Hierarchynet: Hierarchical cnn-based urban building classification. *Remote Sensing*, 12(22):3794, 2020. 2
- [32] Bowen Wang, Jiaxin Zhang, Ran Zhang, Yunqin Li, Liangzhi Li, and Yuta Nakashima. Improving facade parsing with vision transformers and line integration. *Advanced Engineering Informatics*, 60:102463, 2024. 2
- [33] Libo Wang, Shenghui Fang, Xiaoliang Meng, and Rui Li. Building extraction with vision transformer. *IEEE Transactions on Geoscience and Remote Sensing*, 60:1–11, 2022. 2
- [34] Enze Xie, Wenhai Wang, Zhiding Yu, Anima Anandkumar, Jose M Alvarez, and Ping Luo. Segformer: Simple and efficient design for semantic segmentation with transformers. *Advances in neural information processing systems*, 34:12077–12090, 2021. 3
- [35] Ziyao Xing, Shuai Yang, Xuli Zan, Xinrui Dong, Yu Yao, Zhe Liu, and Xiaodong Zhang. Flood vulnerability assessment of urban buildings based on integrating high-resolution remote sensing and street view images. *Sustainable Cities and Society*, 92:104467, 2023. 2
- [36] Joseph Z Xu, Wenhan Lu, Zebo Li, Pranav Khaitan, and Valeriya Zaytseva. Building damage detection in satellite imagery using convolutional neural networks. *arXiv preprint arXiv:1910.06444*, 2019. 2
- [37] Junhan Zhao, Xiang Liu, Yanqun Kuang, Yingjie Victor Chen, and Baijian Yang. Deep cnn-based methods to evaluate neighborhood-scale urban valuation through street scenes perception. In *2018 IEEE third international conference on data science in cyberspace (dsc)*, pages 20–27. IEEE, 2018. 2
- [38] Kang Zhao, Jungwon Kang, Jaewook Jung, and Gunho Sohn. Building extraction from satellite images using mask r-cnn with building boundary regularization. In *Proceedings of the IEEE conference on computer vision and pattern recognition workshops*, pages 247–251, 2018. 2